

Article

Study on the Galvanic Corrosion between 13Cr Alloy Tubing and Downhole Tools of 9Cr and P110: Experimental Investigation and Numerical Simulation

Chuanzhen Zang^{1,2}, Hanqiao Jiang¹, Zongyu Lu², Xianbo Peng^{3,*}, Jian Wang² and Zhanghua Lian³

¹ State Key Laboratory of Petroleum Resources and Prospecting, China University of Petroleum, Beijing 102249, China

² Engineering Technology Research Institute, PetroChina Xinjiang Oilfield Company, Karamay 834000, China

³ State Key Laboratory of Oil and Gas Reservoir Geology and Exploitation, Southwest Petroleum University, Chengdu 610500, China

* Correspondence: pxb19181786943@163.com

Abstract: The galvanic corrosion of oil and gas production string is related to wellbore integrity and production safety. In order to study the galvanic corrosion of an oil and gas well tubing assembly and maintain production safety, this paper studied the galvanic corrosion behavior between 13Cr alloy steel tubing and the downhole tools of 9Cr and P110 in formate annular fluid via experimental and numerical simulation methods. The chemical composition, HTHP corrosion tests and electrochemical measurement of the three materials were investigated to analyze the corrosion mechanism and electrochemical parameters. Then, a full-sized 3D galvanic corrosion model of 13Cr tubing and a 9Cr/P110 joint combination was established using COMSOL Multiphysics software based on the electrochemical test results. The mechanism and current variation law of the galvanic corrosion of different tubing materials are discussed and analyzed in the paper. The results revealed that the corrosion rates obtained based on the electrochemical test are as follows: P110 (0.072 mm/y) > 9Cr (0.033 mm/y) > 13Cr (0.0022 mm/y). The current densities of a combination of 13Cr tubing with a 9Cr joint and 13Cr tubing with a P110 joint vary dramatically: the current density of the 13Cr tubing–P110 joint reach 1.6×10^{-4} A/cm², higher than the current density of the combination of 13Cr tubing and a 9Cr joint. The results of a 3D FEM analysis show that the 13Cr tube demonstrates obvious galvanic corrosion with 9Cr and P110 joints, which is consistent with the analysis results of the polarization curve. This study therefore explains the galvanic corrosion mechanism of different tubing materials and provides guidance for the safe use of tubing in the productive process.

Keywords: galvanic corrosion; 13Cr alloy steel; formate annular fluid; electrochemical test; finite element model



Citation: Zang, C.; Jiang, H.; Lu, Z.; Peng, X.; Wang, J.; Lian, Z. Study on the Galvanic Corrosion between 13Cr Alloy Tubing and Downhole Tools of 9Cr and P110: Experimental Investigation and Numerical Simulation. *Coatings* **2023**, *13*, 861. <https://doi.org/10.3390/coatings13050861>

Academic Editor: Tadeusz Hryniewicz

Received: 12 April 2023

Revised: 26 April 2023

Accepted: 28 April 2023

Published: 30 April 2023



Copyright: © 2023 by the authors. Licensee MDPI, Basel, Switzerland. This article is an open access article distributed under the terms and conditions of the Creative Commons Attribution (CC BY) license (<https://creativecommons.org/licenses/by/4.0/>).

1. Introduction

High-productivity ultra-deep gas wells have progressively drawn the industry's attention due to the potential for their exploration and production activities to accommodate the rapid increase in global energy consumption. However, the service conditions for downhole equipment are very demanding due to the high temperature (HT), high pressure (HP) and corrosive medium, etc. [1–3]. The tubing string, as the sole flow channel, is subject to the combined effects of stress and corrosion; meanwhile, several years of service are also required to ensure normal production. In order to satisfy this requirement, 13Cr stainless steel tubing has been widely used in ultra-deep wells due to its stable mechanical properties and corrosion resistance [4,5]. However, it is worth noting that 13Cr tubing is expensive due to the cost of its production process, while other downhole tool materials, such as 9Cr and P110, are more economical and common. With this in mind, tubing and downhole tools of different materials are often used in different parts of the oil and gas well, such as the

dissimilar metal 13Cr tubing–9Cr joint combination [6]. On the other hand, to avoid tubing corrosion failure during the production process of oil and gas wells, annular protection fluid was often added to the wellbore to mitigate oil and gas corrosion. However, the formate annulus protector is an electrolyte with high conductivity [7,8]. Once the dissimilar metals are simultaneously exposed to the annulus protector and come into contact with each other, there is a potential difference between the different metals due to their different corrosion potentials, which drives electrons from the metal with the lower potential to the metal with the higher potential, resulting in the accelerated corrosion of the anode materials via the galvanic pair. This is generally called galvanic corrosion [9,10]. As underground galvanic corrosion can lead to the early failure of underground pipes in a service period, it is necessary to know the rules of galvanic corrosion between different metals before material selection. Some researchers have investigated the galvanic corrosion behavior between carbon steel and 13Cr stainless steel under different circumstances. Li et al. [11] studied the galvanic corrosion between N80 carbon steel and 13Cr stainless steel under supercritical CO₂ conditions via electrochemical measurements and surface characterization and found that the corrosion of N80 carbon steel was enhanced via coupling with 13Cr stainless steel, and the galvanic current decreases with time due to the formation of a protective FeCO₃ film. Yao et al. [12] studied the galvanic corrosion behavior of a Super 13Cr–P110 steel pair in a NaCl solution via the electrochemical method and found that the galvanic current density generated by the pair would cause serious galvanic corrosion, and the corrosion product was oxide. Wang et al. [13] studied the inhibition effect of a corrosion inhibitor on the galvanic corrosion of N80 carbon steel and 13Cr stainless steel under dynamic supercritical CO₂ conditions and found that inhibitors could effectively inhibit the galvanic corrosion of N80 carbon steel, but the galvanic effect decreases the inhibitive effect of the inhibitors for N80 carbon steel. Zhu et al. [14] studied the corrosion behavior of 13Cr stainless steel under stress and the resultant crevices in a high-pressure CO₂/O₂ environment and found that stress promotes the development of crack corrosion.

Some researchers also have investigated the influencing factors of galvanic corrosion, such as temperature [15], grain refinement [16] and uniaxial tensile stress [17]. Despite many achievements having been made in the study of galvanic corrosion, there are few reports on the galvanic corrosion of tubing materials, especially 13Cr and 9Cr in annulus protection fluid. On the other hand, previous studies mainly focused on experimental methods and rarely combined experiments with numerical simulations. In view of this, this work aims to study the galvanic corrosion between 13Cr tubing and downhole tools constructed of 9Cr and P110 in formate annular fluid using experimental and numerical simulation methods. The chemical composition, HTHP corrosion and electrochemical tests of the 13Cr, 9Cr and P110 materials are first carried out, and some basic parameters are obtained. Then, a finite element model of galvanic corrosion is established and discussed based on the parameters obtained from the test. Finally, the law of galvanic corrosion and the mitigation methods of different combinations of string materials are discussed. A series of important conclusions are drawn in this work.

2. Experimental

2.1. Materials and Experimental Preparation

The tubing and downhole tool materials used in this paper were provided by an oil field. The chemical compositions of the 13Cr, 9Cr and P110 materials were tested according to the national standard, GB/T 4336-2016, and the results are detailed in Table 1. The size of the HTHP (high temperature and high pressure) corrosion testing sample was 40 mm × 10 mm × 3 mm, and the sample was gradually polished using 200~2000-grit SiC paper. Then, the samples were successively cleaned with acetone, deionized water and absolute ethyl alcohol [18].

Table 1. Chemical composition of the tested materials (wt%).

Element	C	Si	Mn	P	S	Ni	Cr	Cu	Mo	V	Fe
P110	0.26	0.24	1.53	0.022	0.003	0.02	0.05	0.07	0.01	0.02	Balance.
9Cr	0.11	0.28	0.51	0.015	0.004	0.15	8.68	0.02	0.96	0.21	Balance.
3Cr	0.16	0.25	0.57	0.012	0.004	0.04	2.92	0.06	0.33	0.01	Balance.

The electrochemical sample was a $\phi 6 \times 10$ mm cylinder. One end of the sample was connected to copper wire via tin welding. The electrode was then encapsulated with high-temperature-resistant paint. The electrode surface was primed, the primer was allowed to dry and then a top coat was applied, several times in turn. After encapsulation, the exposed electrode working surface was a circular surface with a diameter of 6 mm. The electrode surface was polished with 150#, 600# and 800# metallographic sandpaper, and acetone was then used to remove oil. The sample was further cleaned with alcohol, dried in air, and placed in a drying box to be dried before use.

2.2. HTHP Corrosion Tests

In order to reveal the differences in corrosion resistance between the 13Cr, 9Cr and P110 materials, an HTHP cauldron (Southwest Petroleum University, Chengdu, China) was employed to carry out corrosion tests. As shown in Figure 1, the device has a capacity of 5 L, its working temperature limit is 200 °C and its pressure limit is 80 MPa. According to the actual production data collected from the oil and gas well, including the temperature, pressure and partial pressure of CO₂ in the wellbore, the test temperature was 80 ± 0.5 °C, the total pressure was 10 MPa, the CO₂ partial pressure was 0.8 MPa and the test period was 168 h in this work. The corrosive medium was formation water. First, 5 L of formate annulus protection fluid and the samples were placed into the HTHP cauldron and passed through high-purity nitrogen (99.999%) for deoxygenation treatment for 2 h, and the test was then started by heating up and pressurizing the samples according to the test conditions. After the test, the surface of the tubing sample was cleaned with deionized water, dehydrated with acetone, and dried with air. The corrosion products were analyzed via VEGAII TESCAN scanning electron microscopy (SEM) and an Oxford energy dispersive spectrometer (EDS).

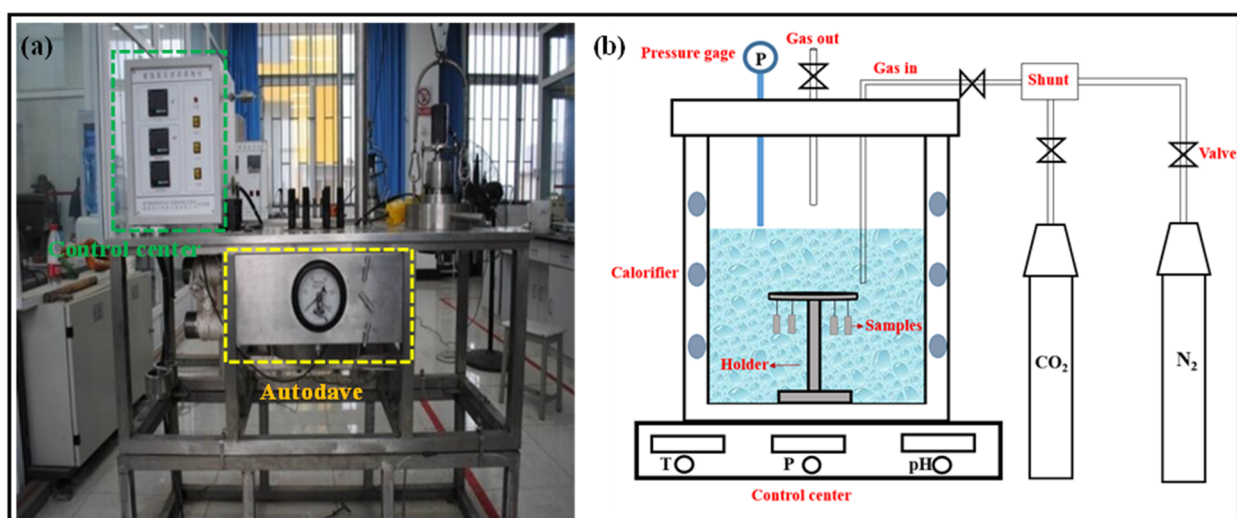


Figure 1. HTHP corrosion test apparatus, (a) HTHP reactor for test, and (b) schematic diagram of experimental principle.

2.3. Electrochemical Measurements

An electrochemical sample, a platinum electrode (Counter Electrode, CE) and a saturated calomel electrode (SCE) were used to construct a three-electrode electrochemical cell [19]. The conductivity of the formate annulus liquid was measured with the conductance instrument DDS-11A. The commercial measurement system, CS350M (Corrtest, Wuhan, China), was set to floating mode for the electrochemical testing. Figure 2 shows the schematic diagram of the electrochemical test. The 9Cr, 13Cr and P110 samples were successively used as working electrodes (WEs). When the open circuit potential stabilized, the polarization curve was measured. The potential scanning range was -500 mV to $+500$ mV, and the scanning rate was 1.0 mV/s. The polarization curve was fitted using the cathode Tafel extrapolation method. The specific performance parameters of the potassium formate annulus are shown in Table 2.

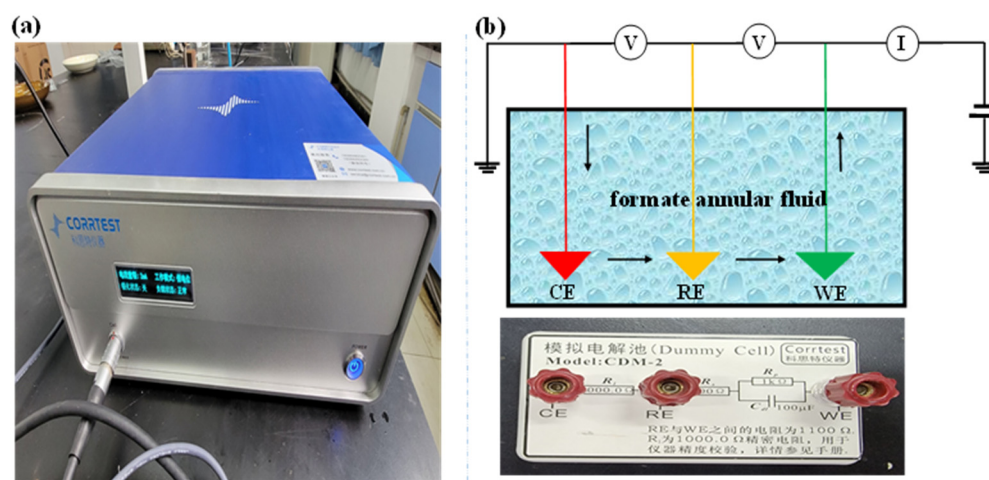


Figure 2. (a) CS350M electrochemical tester and (b) principle.

Table 2. Formate annulus fluid parameters.

Parameter	Value
Saturation concentration (wt%)	49
Density (g/cm^3)	1.45
Funnel viscosity (s)	30
pH	9.8

3. Experimental Results

3.1. HTHP Corrosion Resistance

Figure 3 demonstrates the corrosion morphology and average corrosion rate results of three types of material after corrosion. From a macro perspective, the corrosion of P110 seems to be more serious compared to 9Cr and 13Cr, and 13Cr appears to be the least corrosive. To quantitatively compare the corrosion degree of the three materials, the corroded specimens' corrosion products were removed according to the industry standard ISO 8407-2009, and the samples were weighed using an electronic balance. Then, the loss of weight method was used to calculate the corrosion rate. The weights of the samples before and after the test and the detailed corrosion rates are presented in Table 3. It is clear that 13Cr shows excellent corrosion resistance, with only 0.004 mm/y, but the corrosion rate of P110 is relatively large, reaching 0.6364 mm/y.

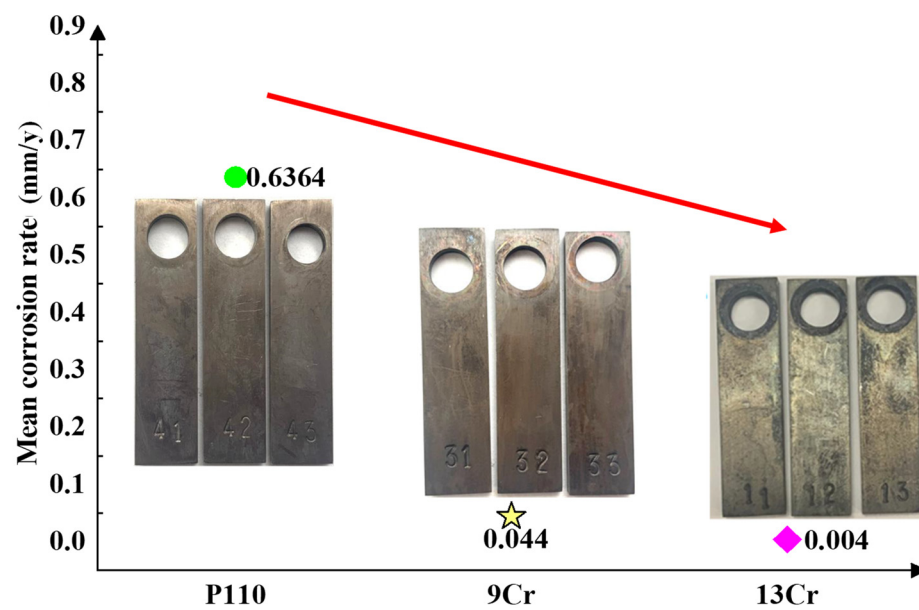


Figure 3. Corrosion morphology and average corrosion rate.

Table 3. The weights of samples before and after the test and the average corrosion rates.

Material	Length (mm)	Wide (mm)	High (mm)	Before Corrosion (g)	After Corrosion (g)	Testing Time (h)	Corrosion Rate (mm/y)	Average (mm/y)
P110	39.69	10.00	3.02	8.4971	8.3922	168	0.6370	0.6364
	39.78	9.76	2.99	8.2001	8.1043	168	0.5932	
	39.61	9.93	2.94	8.3244	8.2142	168	0.6791	
9Cr	39.76	9.95	2.96	8.1980	8.1904	168	0.0465	0.0440
	39.69	9.92	2.92	8.0326	8.0255	168	0.0438	
	39.76	9.95	2.90	8.0023	7.9955	168	0.0418	
13Cr	39.66	9.95	2.98	8.3541	8.3533	168	0.0050	0.0040
	39.72	10.02	2.97	8.3950	8.3944	168	0.0037	
	39.73	9.81	2.98	8.1452	8.1447	168	0.0032	

Figure 4 displays the results of the corrosion morphology and energy spectrum analyses of the three types of material after corrosion, and the second column is the local magnification of the first column. It is clear that the surface of the P110 material is uneven: there are many pitting pits and corrosion products, and the energy spectrum results show that most of these corrosion products are iron oxides. The surface of the 9Cr material is slightly corroded. The 13Cr material has a smooth surface and almost no corrosion marks. When the tubing and downhole tools are working downhole, O₂ from the atmosphere and the wellbore dissolved in the annulus protection fluid will cause a serious electrochemical reaction, and the anodic reaction is as follows [20]:



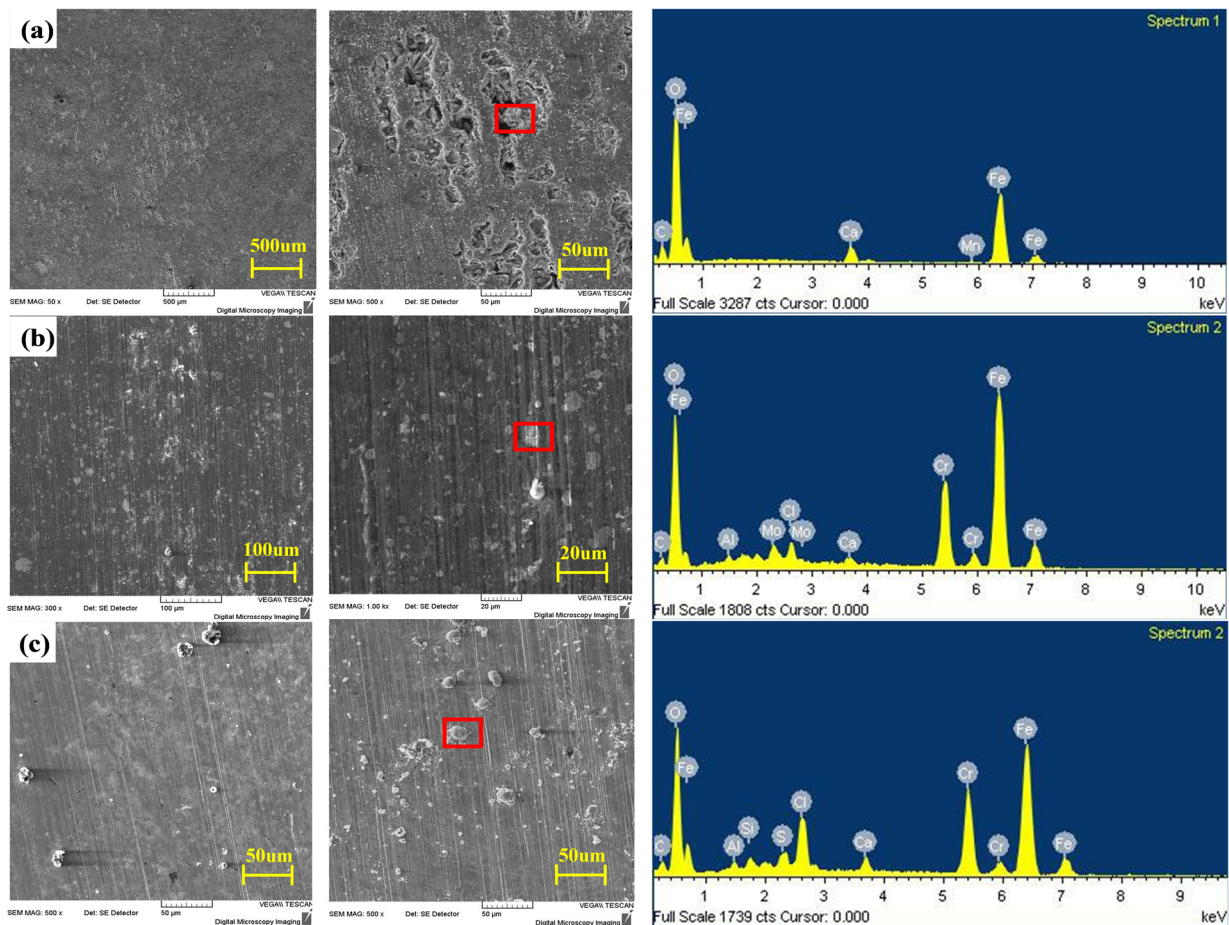


Figure 4. The results of corrosion morphology and energy spectrum analyses of three types of material after corrosion: (a) P110, (b) 9Cr, and (c) 13Cr.

The cathode reaction is:



On the other hand, in a CO_2 corrosion system, the anode process is mainly an iron oxidation reaction. The cathode process is mainly the reduction reaction of the hydrogen ion and carbonic acid:



The reason for the corrosion resistance of 9Cr and 13Cr is that the surface corrosion product $\text{Cr}(\text{OH})_3$ is firmly attached and dense, which plays a good protective role. It is thought that Cr-oxides are generated on the surface of the 9Cr and 13Cr samples, and these oxides could form a dense, passive film to effectively resist the corrosion effect. The main corrosion product of the P110 material is $\text{Fe}(\text{OH})_3$, which is unstable in the high-temperature underground environment and is easily decomposed into Fe_2O_3 and H_2O , failing to protect the matrix inside the material [21].

3.2. Electrochemical Results

Figure 5 illustrates the open circuit potential (OCP) of the three types of material vs. time in the formation environment. It can be seen that the 13Cr is stable at -0.233 V, 9Cr is stable at -0.526 V and P110 is stable at -0.635 V. On the other hand, the PD (potential difference) between 13Cr and 9Cr is 293 mV, and the PD between 13Cr and P110 reaches 402 mV. Based on the corrosion thermodynamics theory, 9Cr and P110 are more prone to corrosion compared with 13Cr; these results were also verified by the HTHP corrosion test. Meanwhile, galvanic corrosion could occur when 9Cr or P110 come into contact with 13Cr under the conditions of a formation environment, e. g. corrosion may occur due to 9Cr's low potential anode in a 13Cr and 9Cr corrosion cell. However, the polarization of materials could occur in electrochemical corrosion, so the measurement of open circuit potential cannot determine whether galvanic corrosion occurs.

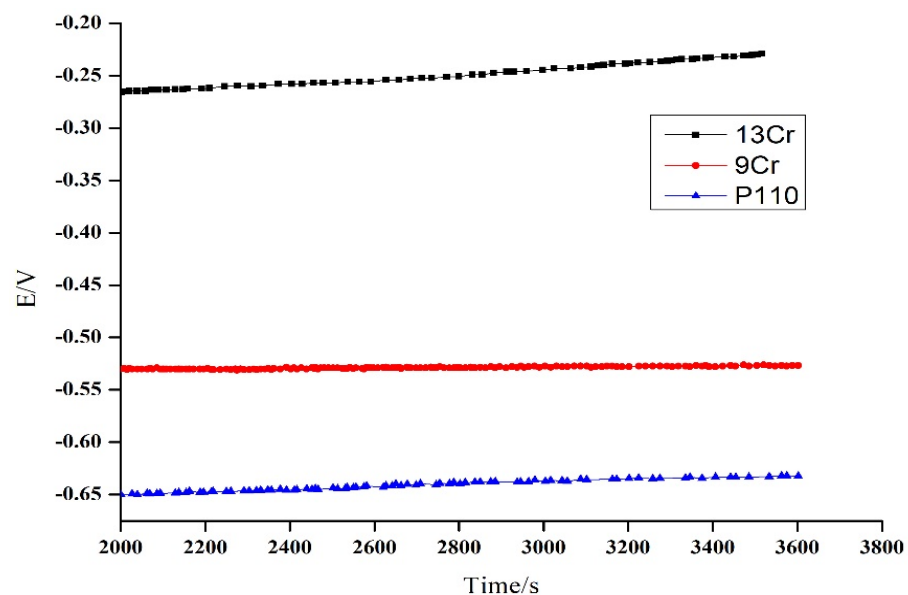


Figure 5. The OCP of three types of material vs. time under conditions of a formation environment.

Figure 6a displays the polarization curves of the three types of material under the conditions of a formation environment. It is worth noting that the E_{cor} and E_{ocp} of the 13Cr and 9Cr materials have slight deviations, which is the result of polarization. It is obvious that the 13Cr material has an obvious passivation zone, and the current does not change with the potential, indicating that 13Cr forms a dense passivation film in the corrosive medium, which is consistent with the observation results of the SEM and also indicates that 13Cr has a good self-passivation ability in the annulus protection liquid system. The polarization curve of 9Cr also has a passivation area, and its passivation potential is more negative than that of 13Cr. However, P110 has the most negative corrosion potential and the highest corrosion current density without an obvious passivation zone. It is clear from Figure 6b that the potential of the three materials changed slightly before and after polarization. The polarization curve represents the relationship between the electrode potential and polarization current. The corrosion potentials of 13Cr, 9Cr and P110 are -0.252 V, -0.543 V and -0.621 V, respectively. The relationship between the corrosion rate and polarization curve is as follows: P110 (0.072 mm/y) > 9Cr (0.033 mm/y) > 13Cr (0.0022 mm/y), which is consistent with the HTHP corrosion test results.

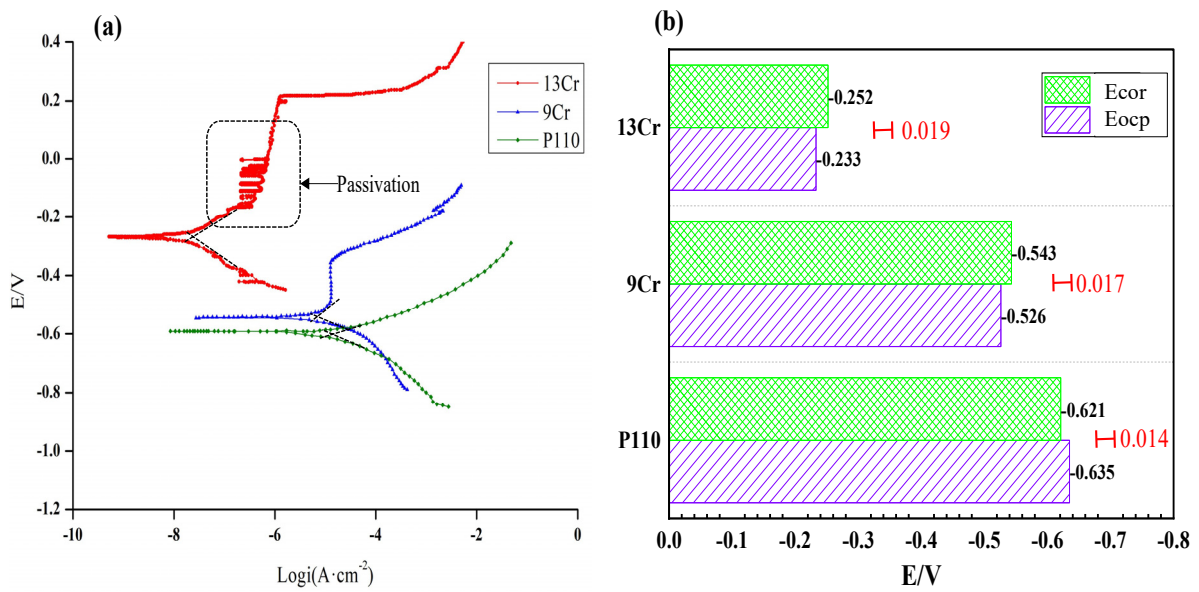


Figure 6. The results of electrochemical test: (a) polarization curves of three types of material and (b) E_{cor} and E_{ocp} of three types of material.

Figure 7 illustrates the open circuit potential of the 9Cr and 13Cr coupling element with different area ratios vs. time in the formation environment. When the two metals are coupled, there is a large potential difference between the 13Cr and 9Cr materials. As the area ratio increases, the potential difference between the 13Cr and 9Cr materials becomes larger. When the area ratio is 1:7, the potential difference reaches 485 mV. The greater the potential difference between them, the more likely it is that galvanic corrosion will occur between the metals. The greater the potential difference, the more likely is metal corrosion. Detailed information for before and after coupling is shown in Table 4. The corrosion rates of different materials before and after coupling are summarized in Figure 8. It can be seen that the corrosion rates of the metals increase with an increase in the area ratio between the coupled metals. When the area ratio is constant, the P110 and 13Cr coupling component is easier to corrode than 9Cr and 13Cr.

Table 4. The corrosion currents of a 9Cr and 13Cr coupling element with different area ratios.

Area Ratio	OCP E_{ocp} (V)		PD (mV)	Current Density (10^{-6} A/cm^2)	Corrosion Rate (mm/y)
	9Cr	13Cr			
1:1	-0.551	-0.1511	399	9.8	0.11
1:3	-0.559	-0.122	437	15	0.174
1:5	-0.562	-0.1051	456	22.8	0.266
1:7	-0.583	-0.098	485	25	0.290

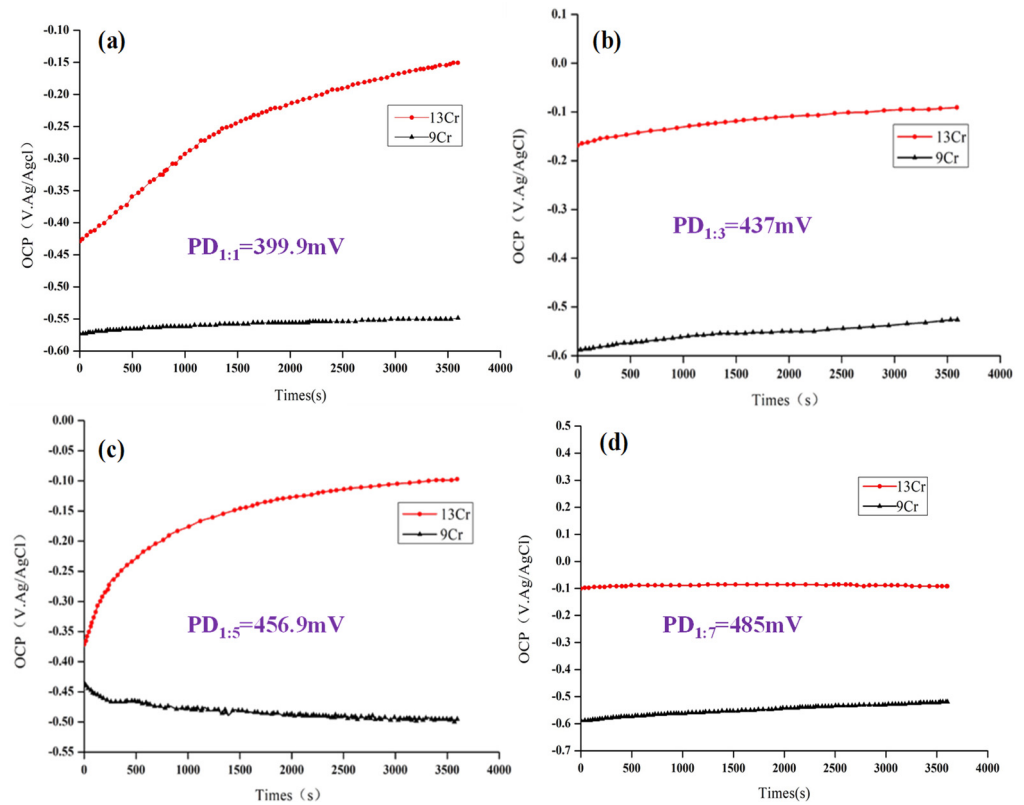


Figure 7. The OCP of 9Cr–13Cr coupling element with different area ratios vs. time in formation environment: (a) 1:1, (b) 1:3, (c) 1:5, and (d) 1:7.

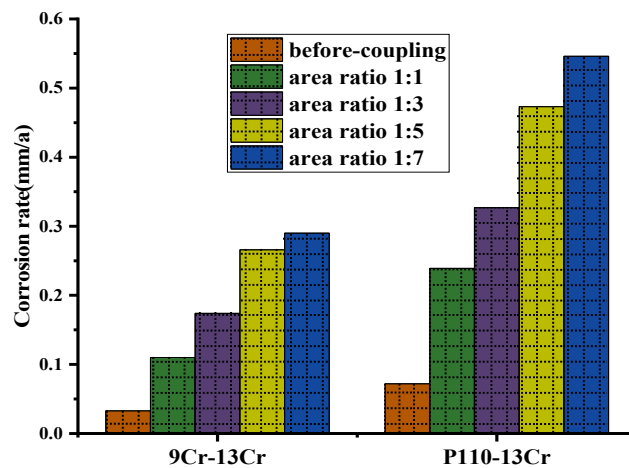


Figure 8. The corrosion current of 9Cr and 13Cr coupling element with different area ratio vs. time in a formation environment.

4. Galvanic Corrosion Modeling

4.1. Modeling

To extend the experimental data of the samples to evaluate the actual corrosion rate according to the actual string size, temperature and corrosive medium, etc., a 3D finite element model (FEM) of the corrosion current field was established to restore the actual corrosion situation between the tubing and dissimilar component using COMSOL® Multiphysics software. Figure 9 shows the FEM of the corrosion current field between the tubing and the dissimilar component and their size. Based on the actual string size, the tubing diameter was set as 88.9 mm, the dissimilar component at 108 mm and the annulus

diameter at 159.42 mm; meanwhile, the length of whole model was 4 m, and the length of the dissimilar joint was 0.5 m.

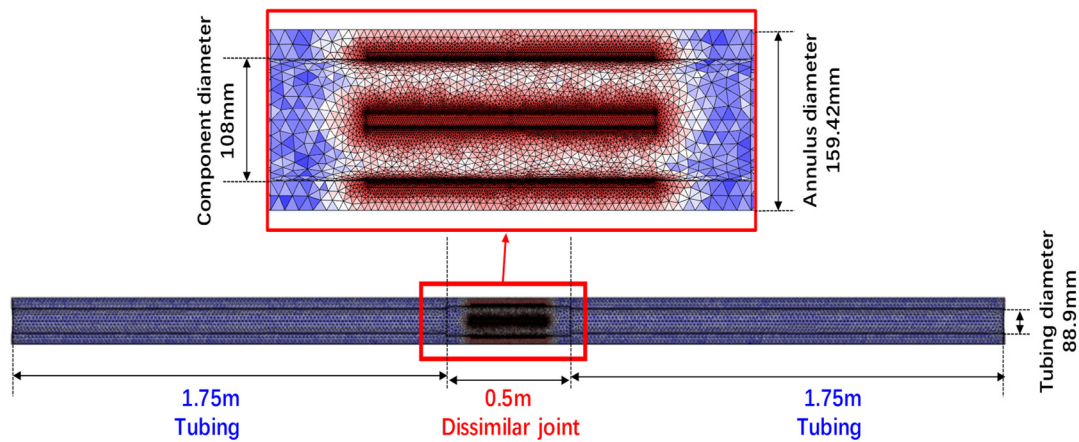


Figure 9. The FEM of corrosion current field between the tubing and the dissimilar joint.

In addition, there were two types of material properties (13Cr and 9Cr/P110) in the whole model, and the attribution of the material properties was set based on the experimental results described in Section 3. The Tafel linear extrapolation method was used to analyze the polarization curves, and the corrosion potential, self-corrosion current density, cathode/anode Tafel slope and other dynamic parameters of the different materials were obtained [22–24].

From the 13Cr corrosion resistance perspective, the equilibrium potential is -0.233 V, the anode and cathode Tafel slope is 27.7 mV/dec, the corrosion potential is -0.252 V and the corrosion current is 0.195×10^{-6} A/cm². Meanwhile, from the 9Cr corrosion resistance perspective, the equilibrium potential is -0.526 V, the anode and cathode Tafel slope is 102.9 mV/dec, the corrosion potential is -0.543 V and the corrosion current is 2.85×10^{-6} A/cm². A free triangular mesh was used for meshing, and a finer mesh was set to improve the resolution of the contact points between the anode and cathode. The experimental polarization data presented above were used to describe the electrode dynamics on the surface of the 13Cr, 9Cr and P110 materials.

4.2. FE Analysis

The contour of the dissolution current density on the inner wall of the combined string (13Cr and 9Cr joint) is presented in Figure 10. It can be seen that the current density is relatively high at the connection region between the 9Cr joint and the 13Cr tubing, and the density reaches 1.44×10^{-4} A/cm². However, the current density is relatively small at both ends of the 13Cr tubing and the intermediate region of the 9Cr joint; the current density is only 4.59×10^{-11} A/cm². Figure 11 shows the contour of the string dissolution current density on the outer wall of the combined string (13Cr and 9Cr joint); the outer current density is slightly lower than the internal, and the maximum current density occurs at the coupling position of the tube body and the joint: 1.44×10^{-4} A/cm². It is important to note that the most severe corrosion of the failed tubing from the oil- and gas-producing well is also located at the junction of the pipe body and the joint, which is consistent with the simulation results.

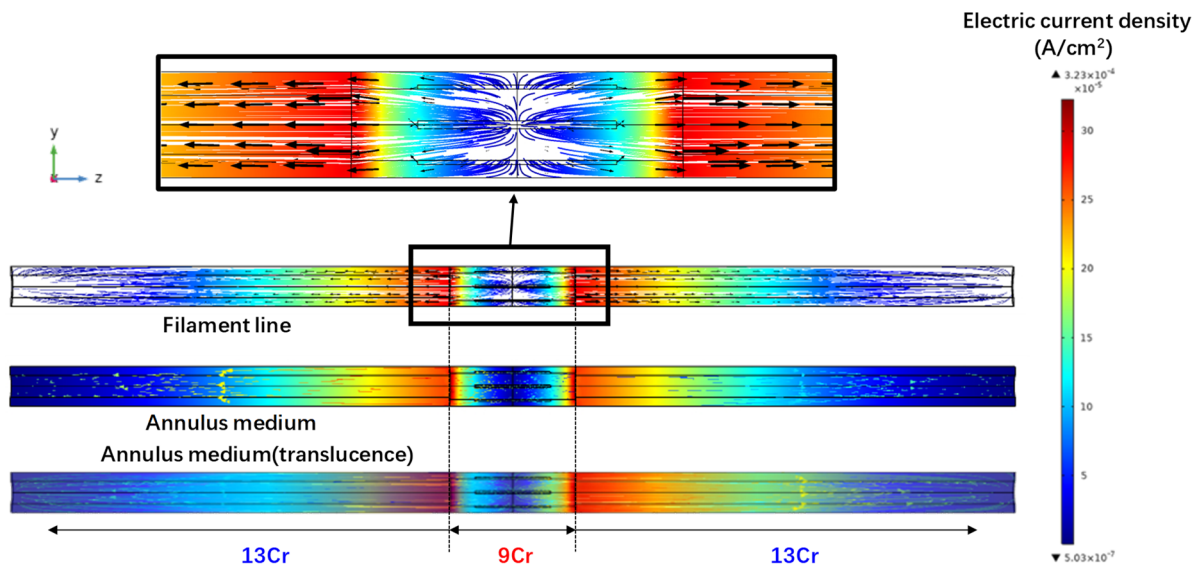


Figure 10. The contour of dissolution current density on the inner wall of combined string (13Cr and 9Cr joint).

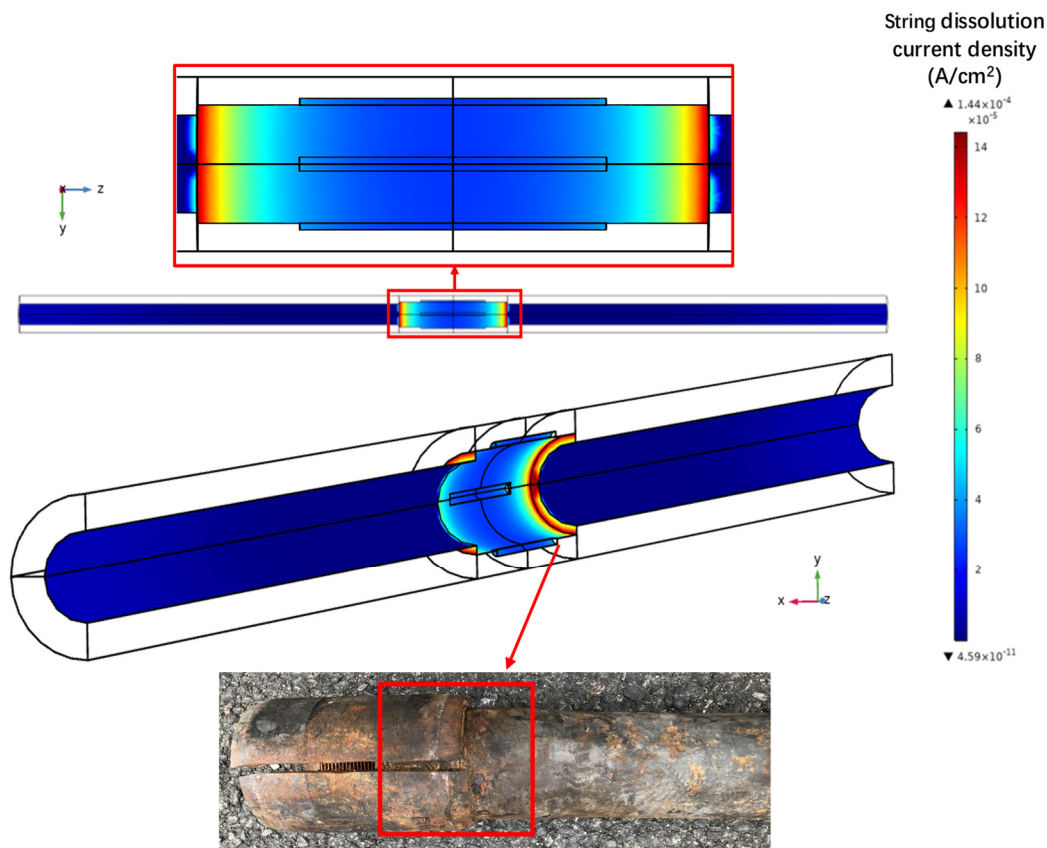


Figure 11. The contour of string dissolution current density on the outer wall of combined string (13Cr and 9Cr joint).

Figure 12 reveals that the current density of the 9Cr and 13Cr coupling component varies with its path, and it was found that the current density varies significantly with the path: the closer the pipe body is to the joint, the higher the current density is, and the maximum value is $1.40 \times 10^{-4} \text{ A/cm}^2$ at the connection position of the pipe body and the joint. From the connection of the pipe body and the joint to the link of the two joints, the current density begins to decline, and it is the smallest at the joint-to-joint section.

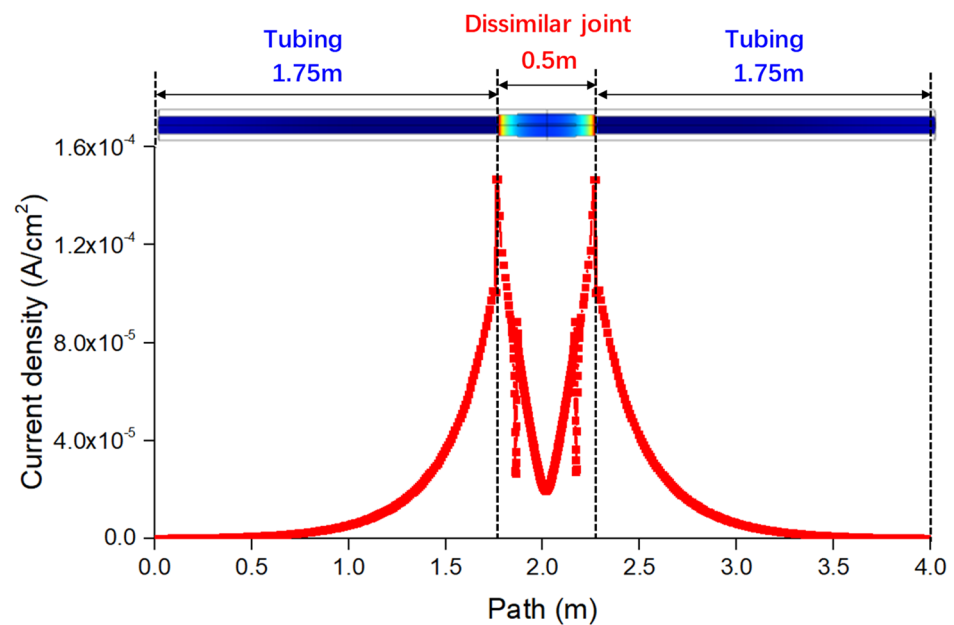


Figure 12. Potential density of 9Cr and 13Cr coupling component varies with path.

5. Discussion

The current density distribution of the P110 and 13Cr coupling component was also studied and analyzed. Figure 13 shows the relationship between the current density and path for different connection materials. When the pipe body and joint materials are both 13Cr, the current density is 0, and there is no galvanic corrosion. It is noteworthy that the current densities of the combinations of 13Cr tubing with a 9Cr joint and 13Cr tubing with a P110 joint vary dramatically; the current density of the 13Cr tubing–P110 joint reaches 1.6×10^{-4} A/cm², which is higher than for the 13Cr tubing and 9Cr joint. The results of the 3D FEM analysis show that the 13Cr tube has obvious galvanic corrosion with 9Cr and P110 joints, which is consistent with the analysis results of the polarization curve. The reason why galvanic corrosion occurs easily in the production process of oil and gas wells is that there is an obvious potential difference between the 13Cr and 9Cr and P110 materials, and different degrees of galvanic corrosion occur when 13Cr is coupled with them. When 9Cr or P110 are used as the anode there is accelerated corrosion, while as the cathode, the 13Cr is protected. Acted upon by tensile and compressive stress, the coupling position fails easily and causes great loss. This study further confirmed the seriousness of galvanic corrosion between 13Cr and 9Cr/P110 tubing string materials. Therefore, in the design of a tubing string for oil and gas wells, it is necessary to consider not only the anticorrosive performance of a single material but also the galvanic corrosion caused by the coupling contact of various materials. It is necessary to select a reasonable combination of tubing to reduce or avoid galvanic corrosion. At the same time, effective anticorrosive measures are formulated to ensure the long-term integrity of the tubing strings of production wells. In light of this, some mitigation measures are proposed for oil and gas production strings:

- (1) Select materials reasonably. The driving force for galvanic corrosion comes from the potential difference between two different metals in contact; hence, the material used for the tubing string assembly should be selected to be as close as possible to the metal in the galvanic sequence. In tubing design, the use of 13Cr–P110 tubing material combinations was avoided as much as possible. Although this saved material costs, it did not pay off in the long run.
- (2) Reasonable structural design. Galvanic corrosion is mainly concentrated near the joint, so when two pipes of different materials are connected through the joint, a structure with a large anode area and a small cathode area should be used as far as possible.

- (3) Protective coating layer. Nonmetallic coatings can be applied to tubing joints to mitigate galvanic corrosion [25].
- (4) Change the corrosive environment. Corrosion inhibitors or cathodic depolarizers can be added to the wellbore to mitigate the corrosive effects of the downhole media.

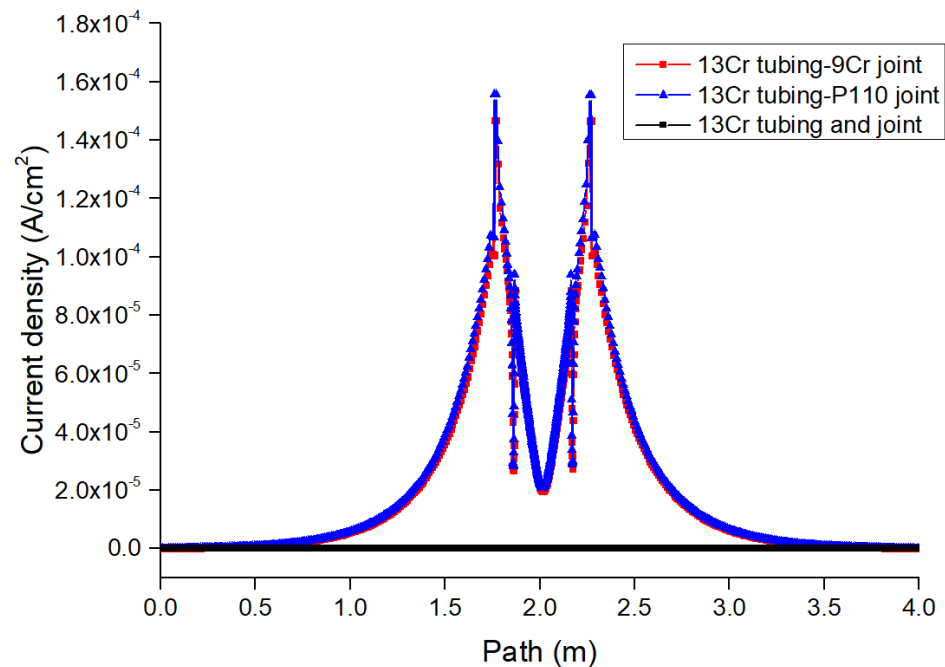


Figure 13. Relationship between current density and path under different connection materials.

6. Conclusions

In this work, the galvanic corrosion behaviors of 13Cr alloy steel tubing strings and 9Cr/P110 downhole tools were studied and discussed. Chemical composition, HTHP corrosion and electrochemical tests of the 13Cr, 9Cr and P110 materials were carried out. Based on the results of the electrochemical tests, a three-dimensional finite element model of the galvanic corrosion of 13Cr tubing with 9Cr and P110 joints was established. The main conclusions can be drawn as follows.

- (1) The HTHP corrosion tests show that the corrosion rates of the three materials in formate are as follows: P110 (0.6364 mm/y) > 9Cr (0.0440 mm/y) > 13Cr (0.0040 mm/y). The electrochemical measurements reveal that the corrosion potentials of 13Cr, 9Cr and P110 are -0.2524 V, -0.5437 V and -0.621 V, respectively. The corrosion rates of the three different materials are as follows: P110 (0.072 mm/y) > 9Cr (0.033 mm/y) > 13Cr (0.0022 mm/y).
- (2) The 13Cr and 9Cr materials have an obvious passivation zone on the polarization curve. The reason for the corrosion resistance of 9Cr and 13Cr is that the surface corrosion product $\text{Cr}(\text{OH})_3$ is firmly attached and dense.
- (3) A 3D FEM of the galvanic corrosion of 13Cr with 9Cr and P110 joints was established based on the electrochemical test results. The FEM analysis shows that the 13Cr tube has obvious galvanic corrosion with 9Cr and P110 joints, which is consistent with the analysis results of the polarization curve.
- (4) When both the pipe body and joint materials are 13Cr, the current density is 0, and there is no galvanic corrosion. It is noteworthy that the current densities of the combinations of 13Cr tubing with a 9Cr joint and 13Cr tubing with a P110 joint vary dramatically, and the current density of the 13Cr tubing–P110 joint reaches 1.6×10^{-4} A/cm², which is higher than the current density of the 13Cr tubing and 9Cr joint.

Author Contributions: Investigation, C.Z. and H.J.; resources, Z.L. (Zongyu Lu); writing—review and editing, X.P.; supervision, J.W.; funding acquisition, Z.L. (Zhanghua Lian). All authors have read and agreed to the published version of the manuscript.

Funding: This research was funded by the National Natural Science Foundation of China (No. 51974271).

Institutional Review Board Statement: Not applicable.

Informed Consent Statement: Not applicable.

Data Availability Statement: Not applicable.

Conflicts of Interest: The authors declare that they have no known competing financial interests or personal relationships that could have appeared to influence the work reported in this paper.

References

1. Yu, H.; Peng, X.; Lian, Z.; Zhang, Q.; Shi, T.; Wang, J.; Zhao, Z. Experimental and numerical simulation of fatigue corrosion behavior of V150 high-strength drill pipe in air and H₂S-dilling mud environment. *J. Nat. Gas Sci. Eng.* **2022**, *98*, 104392. [[CrossRef](#)]
2. Askari, M.; Aliofkhaezrai, M.; Afroukhteh, S. A comprehensive review on internal corrosion and cracking of oil and gas pipelines. *J. Nat. Gas Sci. Eng.* **2019**, *71*, 102971. [[CrossRef](#)]
3. Guo, X.; Liu, J.; Dai, L.; He, Y.; Huang, L.; Wang, G.; Yu, L. Fatigue investigation of tubing string in high-yield curved wells. *J. Nat. Gas Sci. Eng.* **2021**, *85*, 103688. [[CrossRef](#)]
4. Yue, X.; Zhang, L.; Sun, C.; Xu, S.; Wang, C.; Lu, M.; Neville, A.; Hua, Y. A thermodynamic and kinetic study of the formation and evolution of corrosion product scales on 13Cr stainless steel in a geothermal environment. *Corros. Sci.* **2020**, *169*, 108640. [[CrossRef](#)]
5. Svenningsen, G.; Morland, B.H.; Dugstad, A.; Thomas, B. Stress corrosion cracking testing of 13Cr stainless steel in dense phase CO₂ with oxygen. *Energy Procedia* **2017**, *114*, 6778–6799. [[CrossRef](#)]
6. Dong, B.; Zeng, D.; Yu, Z.; Cai, L.; Shi, S.; Yu, H.; Zhao, H.; Tian, G. Corrosion mechanism and applicability assessment of N80 and 9Cr steels in CO₂ auxiliary steam drive. *J. Mater. Eng. Perform.* **2019**, *28*, 1030–1039. [[CrossRef](#)]
7. Zeng, D.; Dong, B.; Zhang, S.; Yi, Y.; Huang, Z.; Tian, G.; Yu, H.; Sun, Y. Annular corrosion risk analysis of gas injection in CO₂ flooding and development of oil-based annulus protection fluid. *J. Pet. Sci. Eng.* **2022**, *208*, 109526. [[CrossRef](#)]
8. Liu, W.; Shi, T.; Li, S.; Lu, Q.; Zhang, Z.; Feng, S.; Ming, C.; Wu, K. Failure analysis of a fracture tubing used in the formate annulus protection fluid. *Eng. Fail. Anal.* **2019**, *95*, 248–262. [[CrossRef](#)]
9. Ostapiuk, M.; Taryba, M.G.; Calado, L.M.; Bienias, J.; Montemor, M.F. A study on the galvanic corrosion of a sol-gel coated PEO Mg-CFRP couple. *Corros. Sci.* **2021**, *186*, 109470. [[CrossRef](#)]
10. Kosaba, T.; Muto, I.; Sugawara, Y. Effect of anodizing on galvanic corrosion resistance of Al coupled to Fe or type 430 stainless steel in diluted synthetic seawater. *Corros. Sci.* **2021**, *179*, 109145. [[CrossRef](#)]
11. Li, Y.; Wang, Z.; Guo, X.P.; Zhang, G.A. Galvanic corrosion between N80 carbon steel and 13Cr stainless steel under supercritical CO₂ conditions. *Corros. Sci.* **2019**, *147*, 260–272. [[CrossRef](#)]
12. Yao, X.; Tian, W.; Xie, F.; Chen, J. Study on Galvanic Corrosion Behaviors of Super 13Cr and P110 Steel Couples in NaCl Solution. *Mater. Rev.* **2017**, *31*, 166–169.
13. Wang, Z.; Li, Y.; Zhang, G. Inhibitive effects of inhibitors on the galvanic corrosion between N80 carbon steel and 13Cr stainless steel under dynamic supercritical CO₂ conditions. *Corros. Sci.* **2019**, *146*, 121–133. [[CrossRef](#)]
14. Zhu, G.Y.; Li, Y.Y.; Hou, B.S.; Zhang, Q.H.; Zhang, G.A. Corrosion behavior of 13Cr stainless steel under stress and crevice in high pressure CO₂/O₂ environment. *J. Mater. Sci. Technol.* **2021**, *88*, 79–89. [[CrossRef](#)]
15. Hu, S.; Liu, R.; Liu, L.; Cui, Y.; Wang, F. Influence of temperature and hydrostatic pressure on the galvanic corrosion between 90/10 Cu–Ni and AISI 316L stainless steel. *J. Mater. Res. Technol.* **2021**, *13*, 1402–1415. [[CrossRef](#)]
16. Wang, P.; Cai, J.; Cheng, X.; Ma, L.; Li, X. Inhibition of galvanic corrosion between crystallographic orientations in low alloy steel by grain ultra-refinement. *Mater. Today Commun.* **2022**, *31*, 103742. [[CrossRef](#)]
17. Anaman, S.; Zhang, S.; Lee, J.; Cho, H.H.; Hong, S.T. A comprehensive assessment of the galvanic corrosion behavior of an electrically assisted pressure joint of dissimilar stainless steel alloys under uniaxial tensile stress. *J. Mater. Res. Technol.* **2022**, *19*, 3110–3129. [[CrossRef](#)]
18. Yue, X.; Zhao, M.; Zhang, L.; Zhang, H.; Li, D.; Lu, M. Correlation between electrochemical properties and stress corrosion cracking of super 13Cr under an HTHP CO₂ environment. *RSC Adv.* **2018**, *8*, 24679–24689. [[CrossRef](#)]
19. Xia, D.H.; Deng, C.M.; Macdonald, D.; Jamali, S.; Mills, D.; Luo, J.L.; Strebl, M.G.; Amiri, M.; Jin, W.; Song, S.; et al. Electrochemical measurements used for assessment of corrosion and protection of metallic materials in the field: A critical review. *J. Mater. Sci. Technol.* **2021**, *112*, 151–183. [[CrossRef](#)]
20. Zhong, X.; Lu, W.; Yang, H.; Liu, M.; Zhang, Y.; Liu, H.; Hu, J.; Zhang, Z.; Zeng, D. Oxygen corrosion of N80 steel under laboratory conditions simulating high pressure air injection: Analysis of corrosion products. *J. Pet. Sci. Eng.* **2019**, *172*, 162–170. [[CrossRef](#)]

21. Raupach, M. Investigations on the influence of oxygen on corrosion of steel in concrete—Part I. *Mater. Struct.* **1996**, *29*, 174–184. [[CrossRef](#)]
22. Yin, L.; Jin, Y.; Leygraf, C.; Birbilis, N.; Pan, J. Numerical simulation of micro-galvanic corrosion in Al alloys: Effect of geometric factors. *J. Electrochem. Soc.* **2017**, *164*, C75. [[CrossRef](#)]
23. Radouani, R.; Echcharqy, Y.; Essahli, M. Numerical simulation of galvanic corrosion between carbon steel and low alloy steel in a bolted joint. *Int. J. Corros.* **2017**, *2017*, 6174904. [[CrossRef](#)]
24. Thébault, F.; Vuillemin, B.; Oltra, R.; Allely, C.; Ogle, K. Reliability of numerical models for simulating galvanic corrosion processes. *Electrochim. Acta* **2012**, *82*, 349–355. [[CrossRef](#)]
25. Burduhos-Nergis, D.; Burduhos-Nergis, D.; Bejinariu, C. Galvanic corrosion behaviour of different types of coatings used in safety systems manufacturing. *Coatings* **2021**, *11*, 1542. [[CrossRef](#)]

Disclaimer/Publisher’s Note: The statements, opinions and data contained in all publications are solely those of the individual author(s) and contributor(s) and not of MDPI and/or the editor(s). MDPI and/or the editor(s) disclaim responsibility for any injury to people or property resulting from any ideas, methods, instructions or products referred to in the content.